Aalto University

Hostikka, Simo; Silde, Ari; Sikanen, Topi; Vepsä, Ari; Paajanen, Antti; Honkanen, Markus

Experimental Characterisation of Sprays Resulting from Impacts of Liquid-Containing Projectiles

Please cite the original version:
Hostikka, S., Silde, A., Sikanen, T., Vepsä, A., Paajanen, A., & Honkanen, M. (2015). Experimental Characterisation of Sprays Resulting from Impacts of Liquid-Containing Projectiles. *Nuclear Engineering and Design*, *295*(December 2015), 388-402. https://doi.org/10.1016/j.nucengdes.2015.09.008

Experimental Characterisation of Sprays Resulting from Impacts of Liquid-Containing Projectiles

Simo Hostikka*, Ari Silde, Topi Sikanen, Ari Vepsä, Antti Paajanen, Markus Honkanen
*) simo.hostikka@aalto.fi

Abstract

Modelling and analysing fires following aircraft impacts requires information about the behaviour of liquid fuel. In this study, we investigated sprays resulting from the impacts of water-filled metal projectiles on a hard wall. The weights of the projectiles were in the range of 38...110 kg, with 8.6...68 kg water, and the impact speeds varied between 96 and 169 m/s. The overall spray behaviour was observed with high-speed video cameras. Ultra-high-speed cameras were used in backlight configuration for measuring the droplet size and velocity distributions. The results indicate that the liquid leaves the impact position as a thin sheet of spray in a direction perpendicular to the projectile velocity. The initial spray speeds were 1.5...2.5 times the impact speed, and the Sauter mean diameters were in the 147...344 μm range. This data can be used as boundary conditions in CFD fire analyses, considering the two-phase fuel flow. The overall spray observations, including the spray deceleration rate, can be used for validating the model.

Introduction

Aircraft impacts have been included in the safety analyses of nuclear power plants (NPP) for a long time, but only recently have these analyses assumed the impact of a large commercial aircraft. The impact of such an aircraft can cause damage to the safety-related structures and components through mechanical impact and fire. Three different modes of influence can be identified in aircraft impact-induced fires: the first mode is a large fireball, caused by the ignition of the aircraft fuel cloud erupting from the breaking fuel tanks. The diameter of the fireball can be tens of metres and it lasts for a few seconds. The second mode of influence is the combustion of residual fuel as a pool fire in the vicinity of the impact location. The size and burning rate of the pool fire depend on the geometry and the properties of the surfaces below the pool. The duration of the pool fire depends on the amount of aviation fuel that did not burn in the initial fireball, the pool burning rate and the possible fire suppression activities. The third mode of fire influence is the penetration of aviation fuel inside the plant through existing openings, or mechanical damage caused by perforated aircraft components. Even if the mass of the penetrated fuel was relatively small, it would cause a rapid ignition of existing internal fire loads, such as electrical cables. Experimental data and simulation capabilities of the high-speed fuel dispersal mechanisms

are needed to develop engineering methods for protection against aircraft impact-induced fires.

Tieszen (1997) has summarised and classified the major fuel dispersal processes in the context of an aircraft crash as follows: the first stage is fuel leakage from the ruptured tank due to the inertial and gravitational forces. Because the deceleration of the plane occurs very rapidly and the impact forces are enormous, the fuel spills out from the ruptured tanks and disperses to surroundings. The next stage is known as the primary break-up phase, where the liquid break-up and atomisation begins, due to the destabilising processes of aerodynamic drag and turbulence within the liquid core. The primary break-up phase is followed by the secondary break-up phase of flying droplets. Due to the interphase momentum transfer from the droplets, the surrounding air is accelerated to a speed that is close to the speed of the spray, and the droplets are decelerated correspondingly. Depending on the speed of a droplet relative to the surrounding gas, the secondary break-up can produce droplets of different sizes. The size distribution resulting from the break-up process can be either uni- or bi-modal in nature. The size and velocity distributions have an influence on the transfer distance of a droplet cloud. The rest of the liquid stream and partially atomised droplets may impact the targets or fall down due to gravitational forces. Flying structures and fragments of the airplane also affect the fuel dispersal processes.

Very few publications are available on full-scale aircraft crash tests including fuel. Early test series by FAA and NACA using belly-landing aircraft demonstrated that fuel spilled from ruptured tanks, forming a fine mist (droplet) cloud that can be ignited by several sources (Pinkel et al. 1953, FAA 1977, FAA 1986). Experiences from numerous real crash incidents, such as the '9/11' terrorist attacks on the World Trade Centre September 11, 2001, support this observation. Furthermore, a film footage analysis of aircraft crash fireballs has indicated that these flame balls are very similar to the fireballs resulting from boiling liquid expanding vapour explosions – i.e. BLEVEs (Luther & Müller 2009). However, none of the analysed accidents included impact on a rigid vertical structure, such as modern NPP.

Most of the published studies involving high-speed impacts of liquids have focused on the fracture and deformations of solid surfaces. The fate of the liquid has been investigated mostly in the length scale of an individual droplet impacting a surface, serving the purposes of process industry and manufacturing technologies, such as spray coating. In his work concerning droplet impacts on rigid surfaces, Knežević (2002) defined 'high-speed' droplet impact as an impact causing at least 5% compressibility in the liquid. This was obtained if the impact speed was in the order of 100 m/s or higher. The properties of the splash have in general been found to depend on the properties of the liquid and the target, air pressure and the initial speed prior to the impact. The velocity of the splashing droplets has been found to be several times higher than the impact velocity (Yarin 2006). Field et al. (1989), for instance, made observations of 10–32 mm droplets hitting various rigid surfaces at a speed of 110 m/s, producing splashing jets with initial speeds of between 670 and 1170 m/s and

splash angles (angle between wall tangent and splash direction) of between 10 and 19 degrees. They observed that a harder target material generally leads to smaller splash angles and higher spray speeds than softer materials.

Experimental scenarios that are qualitatively closer to the aircraft impact are often related to the crashworthiness of the vehicle fuel tanks. Fasanella and Jackson (2001) reported on a drop test of an aircraft fuel tank at speed of about 10 m/s. Anghileri et al. (2005) used various numerical tools, validated through drop tower tests, to investigate the liquid-structure interaction within a tank during impact on the ground. The aim of these studies was to ensure that the fuel tanks can withstand impacts at moderate speeds. They did not increase our knowledge of the fate of fuel in case of tank rupture.

Sandia National Laboratories have conducted a crash test where a Phantom F-4 aircraft carrying 4.8 tonnes of water was hit into a reinforced concrete target at a velocity of 215 m/s (Riesemann et al. 1989, Muto et al. 1989, Sugano et al. 1993). Unfortunately, the liquid dispersal processes were not measured and documented in detail because the main aim of the tests was to study the impact forces versus time. However, the liquid spread process can be seen in the video clips taken from the test (Figure 1). According to the video material, the initial liquid discharge velocity was about 280...330 m/s, i.e. 1.3...1.55 times the impact velocity. The liquid spread pattern seems be quite symmetrical, except the sideward direction. The spread direction calculated from the wall plane was about 0...30° ±10° (0° is along the wall plane, 90° is directly backwards). The final size (diameter) of the cloud was 60...80 m.

Figure 1. Still figures from the video clips of the Phantom F-4 test by Sandia National Laboratories. [1]

Jepsen et al. (2004) investigated the usability of various experimental methods for the diagnostics of high-speed liquid dispersion. In addition to the numerous small-scale tests on individual drops, they discussed the use of photometric, PIV and PDPA measurements in a large-scale water-slug test with a water-filled 1.2 m diameter aluminium cylinder hitting a concrete wall at 105 m/s. The photometrics showed that the initial speed of the radially spreading cloud of water was slightly higher than the impact speed (110 m/s). The cloud in their experiment reached distances of 30–40 m from the impact point. A large-scale PIV, based on the high-speed video images, showed peak velocities of about 250 m/s, i.e.

substantially higher than the values shown by photometrics. A PDPA measurement of the residual spray indicated a size distribution in the range of 6–13 mm, which was concluded to be a result of the secondary break-up or atomisation processes, expecting the break-ups mainly in the bag break-up regime. PDPA measurements did not succeed in capturing the droplets of the primary spray.

BLEVE-induced fireballs are traditionally analysed using analytical and empirical formulas (Abbasi & Abbasi 2007). Such formulas can also be used in the analysis of aircraft impact fires and explosions. In order to take into account the geometrical aspects and details of the event dynamics, it is necessary to use computational fluid dynamics (CFD) tools for the analysis. Using the CFD tools for the task has three major challenges: the first is to collect the necessary input data for prescribing the boundary conditions for the aviation fuel spray. The second challenge is the development of numerical tools with a verified capability to simulate the extremely dynamic reactive flow involving several different length scales. The need to validate the simulation methods and tools forms the third challenge, because the experimental data on impacts with fuel-filled projectiles is not available. The validation must therefore be performed independently for different parts of the modelling methodology, using water-filled projectiles to validate the spray formation and transport calculations, for instance.

The purpose of this work is to contribute to the first and third of the above-mentioned challenges by characterising experimentally the liquid spray resulting from a high-speed impact of a liquid-containing projectile against a hard wall. The intended use of the results is the generation of model inputs and validation data for the CFD simulations of aircraft impact fires. The work has been done in the context of VTT's IMPACT experiments (Kärnä et al. 2004, Lastunen et al. 2007). The paper by Silde et al. (2011) provided an overview of the liquid experiments, but as the experimental methods have been improved from earlier attempts, they will be presented here in detail. The next section describes the experimental methods. The third section presents the experimental results in a form that can be utilised as model inputs (droplet size distribution, initial spray velocity) and validation (spray deceleration). Finally, some concluding remarks will be given.

Experimental methods

Impact facility

The facility for impact testing was designed and constructed in the early 2000s in the wake of the 9/11 terrorist attacks. The facility was initially designed for the measurement of load-time functions generated by soft projectile impacts. Shortly afterwards, the facility was upgraded for testing concrete walls under impact loading. A side view of the test facility is shown in Figure 2. Air pressure is used to accelerate the projectile to its target velocity. Pressure is gradually increased in a pressure accumulator tube (on the left) until it reaches a predefined, test-specific value. The pressure accumulator tube is separated from an

acceleration tube (in the middle) by a flange with a set of plastic membranes taped on both of its sides. When the predetermined value of pressure is achieved, the plastic membranes are punctured and the released air pushes a piston, which is located inside the acceleration tube. The projectile is then pushed forwards by a fin of this piston. The projectile travels on the rails above the acceleration tube. While the projectile continues its flight and ultimately hits the impact plate, the piston is stopped by a piston catcher before it hits the target.

The impact plate is placed between two halves of a steel frame resting on wooden planks. The frame itself is supported in the horizontal direction against the bedrock by four supports, called back pipes.
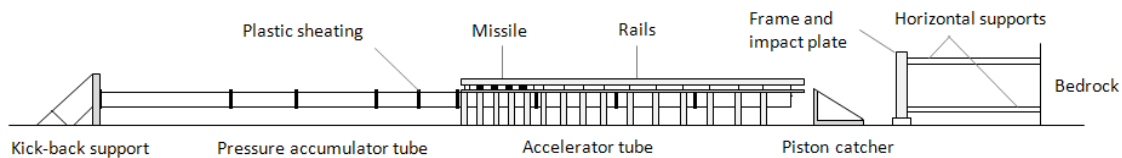
Figure 2. Side view of the impact test facility.

The facility has been designed for projectiles with mass up to 100 kg and diameter between 150–500 mm. Target walls have a square shape with a side-length of 2.1 m. The maximum impact velocity that can be reached depends mainly on the combined mass of the projectile and the piston. For example, with a 50 kg projectile and a 52 kg piston, the maximum speed is currently 165 m/s. A thorough description of the facility is given by Vepsä et al. (2012).

Liquid front observations

Three high shutter speed/high-speed video cameras (1000 frames per second) were used to observe the propagation of the water spray up to 3 m from the impact point. The camera positions within the facility are shown in Figure 3. In three experiments (labelled 632, 652 and FP7), the camera positions differed slightly from those in the figure. At distances beyond 3 m, the liquid flow patterns were affected by the boundaries of the laboratory space. The facility was lit with 48 300 W halogen lamps with a luminous flux of 10 000 lm per lamp. The lamps were arranged in three patterns of 28, 18 and two lamps. In addition, three ETC PAR EA fixtures with 750 W (19 500 lm) HPL lamps were used in two patterns to focus more light on the most important regions of video imaging.
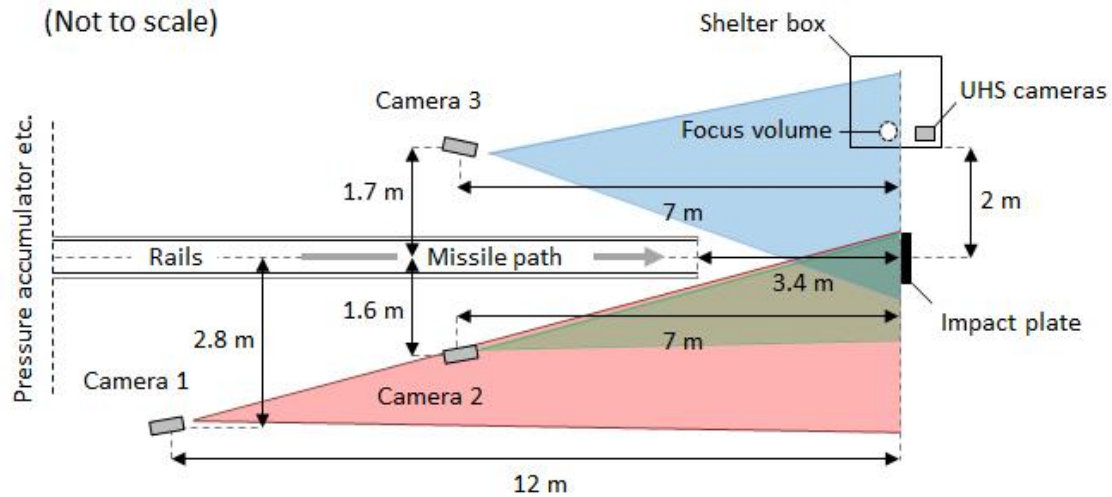
Figure 3. Positions of the regular high-speed cameras and the ultra-high-speed (UHS) cameras. Fields of view of the regular high-speed cameras are indicated by areas highlighted in red, green and blue. The location of the focus volume of the ultra-high-speed cameras is indicated by the white dot.

The radial position of the water front and the spread direction were measured from the still figures taken from the high-speed videos. The water front position was traced in nine different angular directions from the point of impact. Image analysis was used to find the exact location of the front (Figure 4). Since the frame rate of the videos was known, the momentary velocity of the spray front could be estimated from the sequential still figures. The uncertainty of the water front position measurement is estimated to be approximately ±0.1 m or less. This is caused by the factors which hinder clear sight of the water front in the still figures (e.g. limited amount of illumination, minimum available exposure time, limited figure resolution, shadows, mist, other impurities). The uncertainty may also vary slightly in different angular positions and at different moments. Because the period of the sequential still figures is as small as 1 ms, the uncertainty of the spray front position results in an uncertainty in the temporary velocity of the spray front of approximately ±25 m/s, or less. The nearest position where the liquid velocity could be reliably measured was about 0.2 m from the surface of the impacted projectile.

Figure 4. Angular directions where the water front position was measured (left) and an example of measurement in an impact test (right).

The water spread direction looking from the side of the target is also measured from the still figures of the high-speed videos (Figure 5). In this method, a straight line is drawn from the centre line of the ruptured projectile to the leading edge of the water front a few milliseconds after the impact. The spread angle is calculated from the wall plane: 0° is along the wall plane and 90° is directly backwards. The uncertainty of the angular directions is estimated to be ±5° or less.

Figure 5. Examples of the method to measure the water spread direction (side views). Note that each image is taken from a different test.

Spray characterisation

The local spray properties were characterised using two ultra-high-speed digital cameras recording images of flying droplets. The technical challenge of the measurement was related to the wide velocity and size ranges that needed to be observed simultaneously: the spray front was known to consist of large and fast droplets, while the spray following behind mainly consisted of small and relatively slow droplets. One of the cameras was therefore used for measuring the smallest droplets 12-750 μm in diameter, and the other for measuring the larger droplets in the size range of 50-2500 μm. The results of two cameras were combined to a single distribution, noticing the effective measuring volumes of both views.

Sharp still images of droplets were obtained with pulsed high-speed diode laser illumination. Backlight illumination was utilised to obtain images of droplet silhouettes against a bright background. Figure 6 shows the principle of the backlight illumination technique with a camera, backlight and flying droplets that cross the measuring volume. An example of an obtained image is shown on the right.

A schematic drawing of the droplet imaging set-up is shown in Figure 7. The images were taken using two Photron Fastcam cameras (SA-1.1 and SA-X) at frame rates from 40 000 to 100 000 fps and image resolutions from 640 × 208 to 640 × 144 pixels. The cameras have 12-bit 1024 × 1024 pix CMOS sensors with a pixel size of 20 μm. The backlight was produced using Cavilux HF lasers from Cavitar Ltd at 810 nm wavelength and guided through an optical cable to the laser optics. A holographic diffuser was placed between the measurement plane and the laser optics to even out the backlight intensity. The lasers were triggered by the camera frame rate and a 200 ns long laser light pulse was shot once per image frame. The cameras started recording when the trigger signal from the pressure accumulator arrived. Both lasers and the cameras were placed inside a shelter box to protect them from the water spray and flying fragments of the projectile. The shelter box was positioned on the side of the impact position (Figure 3) at distance of 2 m from the centre of the impact position and equipped with a 20 mm-wide vertical gap that allowed a sheet of water spray to enter the measurement volume between the lasers and the cameras. The total distance of the cameras from the centre of the impact point was 2.2 m.

The SA-X camera was equipped with an Infinity K2-S long-distance microscope, including a CF-2 front lens and a 2x optical converter. With 640 × 144 pixel resolution and 100 000 Hz frame rate, this set-up produced a 3.2×0.7 mm^2 field of view at a working distance of 110 mm, which corresponds to the scaling of 5.0 μm per image pixel. Therefore, droplets as small as 12 μm in diameter could be detected. The droplets smaller than 12 μm in diameter were visually observed in the images, but they were not analysed due to high level of imaging noise that disturbed the evaluation of single pixel objects. The depth of field of the

microscopy images was about 4 mm and it halved for micro-droplets with a diameter of less than 30 µm. This means that the smallest droplets (d < 30 µm) where detected only when they were located inside the $3.2 \times 0.7 \times 2.0$ mm^3 focusing range of the SA-X camera.

The SA-1.1 camera was equipped with a Nikon 100 mm macro lens. With 640×208 pixel resolution and a 40 000 Hz frame rate, this set-up produced a 12.8×4.2 mm^2 field of view at a working distance of 130 mm, which corresponded to the scaling of 20.0 µm per image pixel or a magnification of 1.0x. Droplets larger than 50 µm in diameter were successfully analysed from the images of the SA-1.1 camera. Smaller droplets were also clearly visible with 1.0x magnification, but they appeared as 1-pixel dots in the image, whose size could not be evaluated. The lens aperture was set to $f^{\#}$=11 to produce a depth of field of 12 mm.

A novel image analysis algorithm was utilised to detect the individual, in-focus droplets and to track their pathlines. In this method, the edges of the sharp, in-focus droplet images are detected with a Canny edge detector (Canny 1986). An advanced Spoke filter (from Minor & Sklansky 1981) was developed to locate the circular-like droplets based on the greyscale gradient directions along the droplet edge pixels. The region of each droplet image is analysed with a point-spread function approach presented by Fdida & Blaisot 2010. The detected in-focus droplets are tracked over time with an iterative version of the best-estimate tracking algorithm (Ouellette & Bodenschatz 2006), which finds the best match for each droplet in three consecutive image frames. Matching is carried out iteratively to optimise the matching parameters to the current flow conditions (i.e. to the level of turbulence). We assume that the droplet size and the velocity remain unchanged over three image frames (i.e. 20–50 µs period of time).

The measurement set-up was calibrated prior to the measurements by taking images of micro-dots printed on a glass sheet at known depth locations. Images of the micro-dots were analysed with the droplet detection algorithm and the obtained dot size measurements were compared to the known dot sizes. The mean relative sizing error of all detections was 5.0% for high-magnification (4x) images and 3.4% for 1x magnification images. Sizing error increased slightly for smaller dot sizes and when moving the micro-dots away from the focal plane of the imaging system. The maximum sizing error was 10%, whereas the minimum was as small as 0.1%.

The effective depth of field of the imaging system decreased with decreasing droplet size. For both cameras, the smallest recognisable droplets had about one-third of the depth of field of large droplets (0.5–2 mm in diameter). This effect was taken into account by weighting the lowest size classes of the droplet size distributions accordingly.

Figure 6. Principle of backlight imaging.

Figure 7. Schematic drawing of the droplet imaging set-up. The size of the focus volume is greatly exaggerated for illustration purposes.

For spray characterisation purposes, three different mean diameters were calculated from the data. The arithmetic d_{10}, Sauter d_{32} and volumetric d_{43} mean diameters are:

$$d_{10} = \frac{\sum_{i=1}^{N} d_i}{N}, \quad d_{32} = \frac{\sum_{i=1}^{N} d_i^3}{\sum_{i=1}^{N} d_i^2} \text{ and } d_{43} = \frac{\sum_{i=1}^{N} d_i^4}{\sum_{i=1}^{N} d_i^3} \tag{1}$$

Here d_i is the diameter of i:th detected droplet in the image. In addition to the mean diameters, the droplet flux and concentration were also determined. The droplet flux was calculated from the average number of detected droplets per image. The droplet concentration in turn represents the total volume of droplets per total measuring volume and it is presented in ppm.

The main disadvantage of the backlighting is that all the objects that cross the path between the camera and the light are seen in the image. The obtained images contained several blurry droplets that were located either behind or in front of the measuring volume. They hindered the visibility and caused underestimation of the droplet concentration.

Projectiles

The projectiles used in this work can be divided into four categories on the basis of the geometry (cylindrical or cylindrical with added wings) and the material used (aluminium or stainless steel). Table 1 provides the test identifiers of the tests used.

Table 1. The four types of water-filled projectiles according to their test identifiers.

Material ↓/ Geometry →	Cylindrical	Winged
Aluminium	632, 652	688, 689, 695, 696
Stainless steel	FP7, SFP1-5, SFP 7-12	-

Cylindrical projectiles

In total, eight different versions of the cylindrical water-filled projectiles have been used in the tests. These versions differ by material, cross-sectional dimensions, total mass, mass of water, length of water tank and location of water tank.

A typical stainless steel projectile construction is shown in Figure 8 as an example. This construction was used in tests SFP1 - SFP5 and SFP7 - SFP12. The projectile is made of a stainless steel (grade EN 1.4432) pipe (c) with an aluminium 'hat' (d) at the front and a stainless steel cap (b) at the back, to form a water tank. The aluminium hat is pushed inside the pipe and attached with only waterproof padding so that it will yield easily when the projectile hits the steel plate. The steel collar (a) at the back of the projectile is required for pushing the projectile with a fin attached to the piston. The projectiles were designed to

break easily at the front due to internal water pressure and to release the water content into the surroundings. In general, the water tank tends to split into numerous long strips. The number of these strips depends on the ratio between the length of the water tank and its outer diameter, the wall thickness and the impact velocity. An example of a ruptured projectile is shown in Figure 9.

Figure 8. The projectile construction consists of (a) a stainless steel collar, (b) a stainless steel end dome, (c) a hollow stainless steel cylinder and (d) an aluminium front cap.

Figure 9. A projectile after the test.

In addition to the aforementioned differences between the projectile versions, the impact velocity was also varied with roughly three different levels used: ~100, ~125 and ~137 m/s. The main characteristics of the projectiles are listed in d it was completely filled with water.

The spray characterisation failed in tests SFP1, SFP9 and SFP10. In test SFP1, the ultra-high-speed cameras did not trigger. In tests SFP9 and SFP10, the spray front hit the shelter wall so heavily that the gap in the measurement region was closed and only a few droplets arrived in the focus volumes of the cameras.

Table 2 as realised in tests. If not otherwise mentioned, the material of the projectile was stainless steel, the water tank was located at the front of the projectile and it was completely filled with water.

The spray characterisation failed in tests SFP1, SFP9 and SFP10. In test SFP1, the ultra-high-speed cameras did not trigger. In tests SFP9 and SFP10, the spray front hit the shelter wall so heavily that the gap in the measurement region was closed and only a few droplets arrived in the focus volumes of the cameras.

Table 2. The realised values of the projectile parameters in tests SFP1–5 and SFP7–12.

Test id.	Version	Projectile properties					
		Wall thickness	Inner diameter	Water tank length	Mass	Water mass	Impact velocity
		mm	mm	mm	kg	kg	m/s
Tests with spray characterisation							
*SFP2	A	1.5	150	2155	50.52	37.1	97
**SFP3	B	1.5	150	2155	38.09	24.69	97
SFP4	C	1.5	150	1412	38.4	24.81	99
SFP5	C	1.5	150	1412	38.38	24.74	99
SFP7	D	1.5	200	1204	49.75	36.82	103
SFP8	E	2.0	200	1204	51.05	37.24	100
SFP11	D	1.5	200	1204	49.9	36.96	126

SFP12	E	2.0	200	1204	51.5	37	122

<div align="center">Tests without spray characterisation</div>

SFP1	A	1.5	150	2155	50.4	36.96	96
SFP9	D	1.5	200	1204	49.7	36.71	137
SFP10	E	2.0	200	1204	51.1	37.27	137
***632	G	5.0	240	1500	108.1	67.8	96
***652	H	5.0	240	~630	50.7	28.0	104
****FP7	I	3.0	250	559	51.93	24.66	135

*	In test SFP2, a camera with 4x magnification malfunctioned.
**	In test SFP3, the water tank was only filled to two-thirds of its volume.
***	In tests 632 and 652, the material of the projectile was aluminium.
****	In test FP7, the water tank was located at the centre of the projectile, 338 mm from the front. The impact velocity of the tank was roughly 102 m/s.

Winged projectiles

In addition to cylindrical projectiles, a projectile type that represents a whole aircraft was also designed. The purpose of these 3D projectiles was to incorporate the wings and the knife effect they may cause. A schematic drawing of the winged projectile is shown in Figure 10. The projectile consists of a hollow, thin-walled cylindrical pipe simulating the fuselage of an aircraft, a trapezoidal thin-walled box below the pipe, simulating the wings, 200 mm-long 'claws', made out of 3 mm-thick steel sheets, below the wings, and a separate thick-walled steel pipe at the back. The purpose of the 'claws' was to keep the projectile on the rails of the launch pad during acceleration. The back part was added to increase the weight of the projectile. Both the projectile body and the wings were made of aluminium. The wings were made watertight and filled with water to simulate the fuel inside the wing tanks of an aircraft. These wings/water tanks tend to break into three large and a few smaller parts in the tests, as shown in Figure 11. The main dimensions of the projectile, referred to in Figure 10, are as follows:

- projectile length: l_p = 1130 mm,
- span width: W = 1300 mm,
- length of the wings: l_w = 350 mm,
- starting location of the wings: 350 mm from the front,
- inner diameter of the pipe: D_p = 200 mm,
- thickness of the pipe wall: t_p = 4 mm,
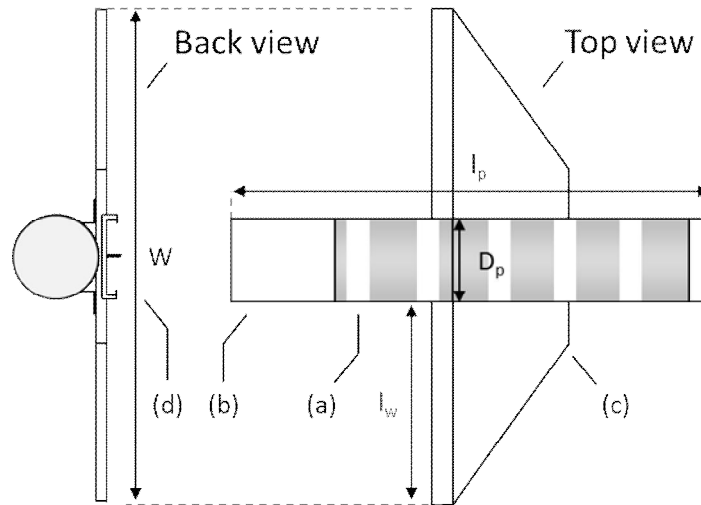- thickness of the wing material: t_w = 3 mm.

Figure 10. Main components of the 3D projectile construction: the (a) aluminium pipe, (b) steel pipe section, (c) aluminium wings, and (d) steel claws.

Figure 11. A 3D projectile after test 688.

The test-specific values of the projectile mass, water mass, impact velocity and the estimated impact velocity of the water tank are shown in Table 3. The impact velocities of the water tank are lower than the projectile velocities because the wings were placed at a finite distance from the projectile front, and because the projectiles decelerated before the wings hit the impact plate. The impact velocities of the wing tanks were estimated assuming a constant rate of deceleration, knowing the impact duration when similar projectiles without wings were used.

Table 3. The realised values of the projectile parameters in tests with winged projectiles.

Test ID	Mass	Water mass	Impact velocity	Impact velocity of the water tank
	kg	kg	m/s	m/s
688	41.15	9.05	137	118
689	40.65	8.6	142	124
695	40.36	8.6	167	149
696	41.08	9.4	169	151

Results and discussion

Spray imaging

Images of a typical liquid dispersion pattern from a cylinder projectile at three separate moments are illustrated in Figure 12. The images were taken from test SFP5, where the impact velocity and the amount of liquid were 100 m/s and 25 L, respectively. High-speed

liquid droplets and jets form stripes in the images due to the motion blur, especially in the vicinity of the projectile. The liquid dispersion occurs quite uniformly in all directions around the projectile, but the projectile fragments may cause perturbations of the liquid front, possibly increasing the folding and fingering of the front. As a result, the spray front can propagate at different velocities in different directions. In some directions, there are fragments impeding the spray propagation. There is also an issue with the projectile leaning to one side, leading to the faster spray front propagation in the opposite direction. The far-field images from test no. 652 show the liquid spray dispersing as several radial waves (Figure 13). The propagation speeds of the sequential waves are approximately equal near the impact location, but later, the leading front of the cloud decelerates strongly and some waves coming from behind may pass the leading front. Based on the current data, it is not possible to definitively conclude whether the waves are produced during the eruption from the breaking tank or as a result of liquid-gas interactions.

Figure 12. Near-field liquid dispersion pattern in test SFP5 with an impact velocity of 100 m/s and 25 L of water. The time instances are 1, 2 and 5 ms after the impact.

Figure 13. Far-field liquid dispersion pattern in test no. 652 with an impact velocity 100 m/s and 28 L of water. The time instances are 2, 6 and 10 ms after the impact.

A typical dispersion pattern from a winged projectile (impact velocity 137 m/s) is shown in Figure 14. The total amount of water locating inside the wings was 8 L, with the cylindrical part of the projectile being empty. When the wings hit the wall, the leading edges of the wings are first ruptured open, and the liquid dispersion occurs primarily in vertical directions (i.e. in the normal directions of the wing surfaces). Compared to the cylindrical projectile tests, the vertical spread directions are pronounced, and only an insignificantly small amount of water is ejected sideways. This conclusion is also confirmed by images from another winged projectile test, where the impact velocity was 167 m/s (Figure 15). The observed behaviour is consistent with the video material from the SNL Phantom F-4 experiments.

Figure 14. Near-field liquid dispersion pattern from 3D projectile test no. 688 with an impact velocity of 137 m/s and 8 L of water. The time instances are 1, 3, and 5 ms after the impact.

Figure 15. Far-field liquid dispersion pattern from 3D projectile test no. 695 with an impact velocity of 167 m/s and 8 L of water. The time instances are 1, 5 and 10 ms after the impact.

The earlier Phantom F-4 and cylinder experiments, conducted by SNL, have revealed that the liquid dispersion starts along the wall plane and a flat dispersion pattern is formed

around the target (Riesemann et al. 1989, Sugano et al. 1993, Jepsen et al. 2004). Side view images from selected tests of the current campaign show similar behaviour (Figure 5 and Figure 16). The ejection angle of the liquid, measured near the projectile, is in the range of 20...40° from the wall plane. This result was obtained for both the cylindrical and winged projectiles. Further away from the impact location, the spray angle is usually smaller. We assume that the spray angle is reduced over the course of the spray movement due to the one-sided air entrainment. Air entrainment is a fluid dynamic process of jets and plumes, where the viscous stress between the primary flow direction and the surrounding gas causes the movement of the gas towards and along the jet or the plume. In the impact scenario, the air can only be entrained into the spray from the direction of the arriving projectile, and horizontal momentum occurs only towards the wall. As a result, the spray is 'pushed' towards the wall, and the spread angle becomes smaller than what it is initially.

Figure 16. Side view images of liquid dispersion pattern in selected VTT impact tests (note that each image is taken from different tests).

Figure 17 shows the measured spray front velocities as a function of the distance from the projectile surface. Figure a) shows the velocities from tests SFP1-SFP12, i.e. with two different projectile diameters and different impact velocities. Each curve represents the median over the angular directions shown in Figure 4. The differences between the velocities measured from individual tests are slightly bigger than the measurement uncertainty. In Figure 17 b), the velocities from three selected tests are normalised by dividing the spray front velocity with the projectile impact velocity.

$$V^* = V_{\text{spray}} / V_{\text{impact}} \tag{2}$$

Correspondingly, the distance from the impact position is normalised with the projectile diameter

$$R^* = R / D \tag{3}$$

In most experiments, the highest spray velocities ($V^* \geq 2$) were obtained near the impact position. In some tests, however, the behaviour of the spray front velocity was not consistent, as illustrated in Figure 17. The overall results indicate that the spray front velocity decreases as the time and distance from the impact target increase. In the tests presented in Figure 17 b), the spray front decelerates to a level of projectile impact velocity ($V^* = 1$), first at $0.5 < R^* < 1$, but then it accelerates again. The spray front velocity fluctuations can, at least partially, be caused by the measurement uncertainty, but they can also be explained by the sequential waves of the spray: if the leading front decelerates enough, the following wave with a higher velocity may pass. This can be seen as a velocity jump, presented in Figure 17.
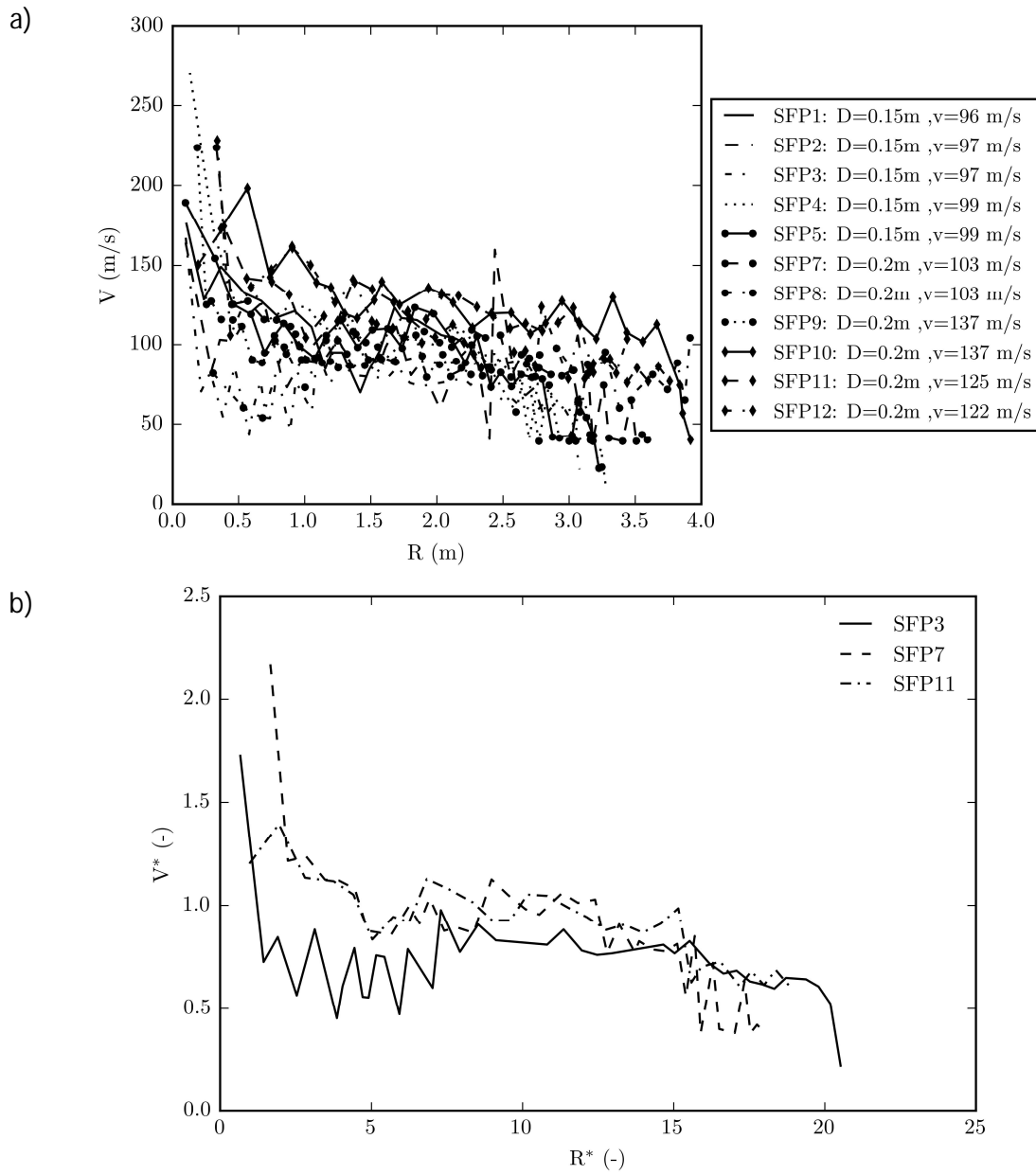
a)

b)

Figure 17. Spray front velocities of tests SFP1-SFP12 (a), and the normalised velocities of three selected tests (b).

Figure 18 presents the normalised liquid front velocities in the region very close to the projectile in selected impact tests. In addition to the median values, average values with error bars indicating the standard deviation and the maximum measured values are plotted. The measurements indicate that the liquid velocity near the projectile is much higher than the impact velocity. Velocity ratios as high as 3–4 were detected in some tests, but mostly the average and median velocity ratios close to the impact point are between 1.5 and 2.5. The results also indicate that the velocity ratio is quite independent from the projectile impact velocity.

Figure 18. Liquid front velocity near the projectile: median, average with error bars indicating the standard deviation and maximum values.

The spray front velocity data is summarised in Figure 19. Each marker represents an average velocity from an individual test at a single distance. By linear extrapolation, the initial spray velocity becomes 1.7 ± 0.25 times the impact velocity, and the velocity decreases to the level of the impact velocity at distance R* » 4.

Figure 19. Normalised velocity as a function of normalised distance from the impact location.

Droplet imaging

Images from the ultra-high-speed video cameras were used to analyse the general characteristics of the spray, droplet velocities and drop size distributions. When analysing the results, one must remember that the images were taken inside the protective box after the flow had entered through a 20 mm gap, which allowed only a small proportion of the spray to enter the measurement region. Both the radial spread and the ejection angle of the spray affected the amount of water that entered the measurement region.

Figure 20 shows three individual images of the spray passing by the SA-1.1 camera in test SFP11. The first image was taken 0.6 ms after the first droplets were observed, representing the early part of the spray. The second image was taken 0.4 ms later and already represents a very dense part of the spray. Dozens of droplets could be detected from this image using the image analysis software, although with the naked eye it is difficult to observe any droplets at all. The third image was taken 24 ms after the arrival of the spray. It represents the bulk of the spray. Figure 21 shows three images from test SFP12, taken by the SA-X camera. In these images, the initial spray front is seen as a dark area consisting of both in-focus and out-of-focus droplets.

Figure 20. Images from the ultra-high-speed video (larger image area) of test SFP11.

Figure 21. Images from the ultra-high-speed video (smaller image area) of test SFP12.

Table 4. Average droplet speed and size as function of projectile parameters.

Test ID	Water mass	Wall thick-ness	Impact velocity	Max. droplet velocity	Peak mean droplet velocity	Peak RMS droplet velocity	d_{10}	d_{32}	d_{43}
	kg	mm	m/s	m/s	m/s	m/s	μm	μm	μm
SFP2	37.1	1.50	97.3	107	63.4	24.4	96	208	262

SFP3	24.7	1.50	96.6	103	39.0	12.3	78	180	152
SFP4	24.8	1.50	98.7	103	51.3	19.5	61	147	116
SFP5	24.7	1.50	99.3	101	24.0	14.8	55	153	190
SFP7	36.8	1.50	103	116	34.4	19.4	67	344	254
SFP8	37.2	2.00	99.7	100	26.3	18.4	53	253	183
SFP11	37.0	1.50	126	130	54.6	27.8	39	316	372
SFP12	37.0	2.00	122	127	43.3	24.0	49	237	223

Table 4 shows the main spray characteristics for test SFP2-SFP12. The droplet velocities are reported as the maximum velocity, the peak of mean velocity and the peak of rms velocity. Time series of the mean velocities and the rms velocities were computed with 15 ms time classes. The peak values of the mean and rms droplet velocities correspond to the maxima of these time series. Maximum droplet velocity is the maximum velocity of an individual droplet observed in the test. The mean droplet size is reported as the arithmetic mean, Sauter mean and the volumetric mean over the whole measurement period.

The maximum and peak mean droplet velocities are plotted as a function of the impact velocity in Figure 22. There is almost no correlation between the average droplet velocity and the impact velocity, whereas there is an almost perfect correlation between the impact velocity and the maximum observed droplet velocity. The maximum observed droplet velocities most likely belong to large liquid fragments that are relatively sparse in the spray. Their effect on the average velocity is therefore very small. The average value is dominated by the small droplets, which in turn are likely to travel at velocities that are very close to their terminal velocities. The observed mean droplet velocities are thus heavily influenced by the local gas phase velocities. As far as the projectile wall thickness has any effect, the current sample size is too small for detecting this effect.

Figure 22. Effect of impact velocity on measured droplet velocities. The maximum observed particle velocity on the left and the peak value of mean droplet velocity on the right.

Droplet size distributions

Figure 23 shows the time histories of the three mean diameters and the spray number concentration in three of the tests. The time in these figures starts when the spray front arrives in the measurement location. In all three tests, the initially high number concentration is followed by a long, relatively diluted tail. The number mean diameter d_{10} shows a flat or decreasing trend for the three examined tests. The trends for the volume-weighted means d_{32} and d_{43} show a greater variance. The variance is lower for approximately the first 50 ms of observations. This phase is followed by a noisy phase indicating heterogeneous spray consisting of secondary spray fronts, residual mist and large water fragments. Both d_{32} and d_{43} place more weight on the large droplets. They are thus more sensitive to the existence of large liquid fragments, which can cause fluctuations in the resulting time series. In our experiments, even the smallest observed mean diameters were

larger than the SNL results for the diameters of the residual mist droplets, being in the range of between 6 and 13 mm.

The plots in Figure 24 show the time histories of the droplet velocity and the normalised cumulative mass flux in three selected tests. The normalised cumulative mass flux is calculated using the average droplet velocity and the measured concentration. The result is normalised using the accumulated observed mass from the whole duration of the measurements. This quantity can be used to approximate the fraction of the total spray volume that is contained by the various stages of the spray. In the three tests, between 60 to 90% of the spray mass passes the measurement location during the first 50 ms. The fluctuating parts of the diameter time series in Figure 23 are thus related to the residual parts of the spray containing relatively little mass.

Figure 23. Mean, Sauter mean, volumetric mean droplet diameters and the spray concentration as a function of time for three selected tests. Time starts from the moment the spray front arrives at the measurement location.

Figure 24. Trends of measured droplet velocity at measurement location. Top left: maximum droplet velocity, top right: average droplet velocity. Bottom left: variance of droplet velocity. Bottom right: Normalised accumulated mass of water.

The classical approach for modelling the droplet size distributions is to fit an analytical distribution to the experimental data. Several choices for the droplet size distribution are available in the literature (see e.g. Babinsky, 2002). Here we focused on three different analytical distributions: Rosin-Rammler distribution, the log-normal distribution and the combination of the Rosin-Rammler and log-normal distributions. These three distributions were chosen because they are available for modelling the droplet size distributions in the CFD software Fire Dynamics Simulator, which is commonly used in the fire safety engineering community (McGrattan et al. 2012).

The Rosin-Rammler distribution was originally developed for modelling the size distribution of the coal particles, but has been widely used for modelling spray droplet size distributions (Babinsky, 2002). The log-normal distribution is usually considered as a model for the cumulative number fraction (CNF). Here it is used as a model for the cumulative volume fraction (CVF) instead. The combination of these two distributions, called Rosin-Rammler-lognormal distribution, has been found to describe the droplet sizes in sprinkler sprays, and is commonly used among fire safety engineers.

Rosin-Rammler distribution:

$$F(d) = 1 - exp\left[-0.693\left(\frac{d}{d_m}\right)^{\gamma}\right] \tag{4}$$

Log-normal distribution:

$$F(d) = \frac{1}{\sqrt{2\pi}} \int_0^{d'} \frac{1}{\sigma d'} exp\left[-\frac{log\left(\frac{d'}{d_m}\right)^2}{2\sigma^2} \right] \tag{5}$$

Rosin-Rammler-Log-normal combination:

$$F(d) = \begin{cases} 1 - exp\left[-0.693\left(\frac{d}{d_m}\right)^{\gamma} \right] & , d > d_m \\ \frac{1}{\sqrt{2\pi}} \int_0^{d'} \frac{1}{\sigma d'} exp\left[-\frac{log\left(\frac{d'}{d_m}\right)^2}{2\sigma^2} \right] & , d \leq d_m \end{cases} \tag{6}$$

where d_m is the volumetric median diameter of the size distribution (half of the volume of the particles is in droplets smaller than this).

In the analysis, the first 15 ms of the observations were assumed to belong to the spray front. Using this definition, the spray front contained approximately 20% of the total mass of the spray (approximated from measured volume fractions). The continuous spray is the rest of the spray. The resulting size parameters are shown in Table 5.

Figure 25 compares the fitted volumetric density distributions with the experimental data that was combined from all the experiments. The fitted distribution functions cannot capture all the features of the experimentally determined distributions. In particular, the experimental distributions have a sharp spike at the small particle diameters, followed by a long tail. The log-normal distribution function can reproduce this behaviour most accurately. The Rosin-Rammler distribution significantly over-predicts the number of very small particles. In experiments SFP2-7, the continuous part of the spray contained large droplets, which increased the estimates of the volumetric median diameter d_m.

Table 5. Fitted distribution parameters.

		Distribution					
	Experiment	Rosin-Rammler		Rosin-Rammler-Log-normal		Log-normal	
		d_m (µm)	γ	d_m (µm)	γ	d_m (µm)	σ
SFP 2-5	Whole	80	0.89	78	0.86	77	1.12
	Front	90	1.03	87	0.98	85	0.98
	Continuous	80	0.87	78	0.85	77	1.14
SFP 7-12	Whole	101	1.04	99	1.01	98	0.96
	Front	84	1.42	82	1.33	80	0.76
	Continuous	105	1.01	103	0.98	101	0.98

	Whole	85	0.93	83	0.89	82	1.08
All	Front	88	1.09	85	1.03	84	0.94
	Continuous	86	0.90	84	0.87	83	1.10

Figure 25. Comparisons of fitted distributions with experimental data. On the left: probability density functions. On the right: cumulative density functions. Continuous lines show the experimental distributions averaged over all experiments. Dashed lines show the fitted distributions.

The droplet size results can be analysed in the light of the existing literature of the spray atomisation process. The most important parameter for the droplet formation is the relative speed between the liquid and the surrounding gas. Although convenient for computational models, this parameter is difficult to determine from experiments where the observations are made for absolute droplet velocities without the knowledge of the speed of the gas moving along the spray. In the impact scenario, the spray front is penetrating into the (practically) still air, and thus the spray front speed measurements can be used to estimate the largest possible stable droplet size. According to one of the commonly used theoretical models for the secondary break-up (Reitz 1987), the stable water droplet size at the speed of 170 m/s (corresponding to the initial spray from an 100 m/s impact) is about 30 mm. The 1 mm-sized droplets in the spray front statistics (Figure 25) can be seen as an indication of much lower relative speeds (as low as 30 m/s). Alternatively, it can mean that the break-up process is unfinished, and the observed distribution is still developing. Indeed, the shapes of the first water fronts in Figure 20 and Figure 21 indicate that the water is still in the form of large fragments, not a mist consisting of spherical droplets. As the time scale of the break-up process (~ 1 ms) is shorter than the travel time from the impact position to the measurement location (~ 20 ms), the existence of large droplets at the measurement location indicates a complicated flow phenomenon where the first front of water always enters still air, meets a high drag and is then broken down to relatively small droplets of a few tens of microns. The momentum of these small droplets is low, and they are quickly decelerated and eventually passed by larger, faster-moving droplets. At the same time, the air speed within the impact spray is accelerated and the relative speed of the droplets leaving the impact position behind the initial front is significantly lower than the relative speed at the first front. The existence of the different droplet velocities is demonstrated in Figure 26, which shows a sequence of images where two droplets (highlighted by the arrows in the first image) collide with a relative velocity of 20 m/s. The collision is caused by the velocity difference, and it is found to create plenty of micro-droplets. The time between each image is 20 ms.

Figure 26. Collision of two droplets with a velocity difference of 20 m/s (in SFP5). Time between each image is 20 ms.

Despite the uncertainties associated with the measured spray characteristics, the measured distributions can be used to serve as boundary conditions for the CFD analyses of the liquid spreading from impact scenarios. Making an analysis of the aircraft impact fires naturally requires a consideration of the effect of the liquid type on the spray formation process. However, the geometrical and other variations of the real impact scenarios are likely to dominate the uncertainties over the difficulties of prescribing droplet size and speed distributions for fuel droplets.

Conclusions

In this article, we presented the experimental characterisation of liquid sprays resulting from high-speed impacts of liquid-filled projectiles against a hard wall. The experiments were carried out using water-filled aluminium and stainless steel projectiles at speeds of between 96 and 169 m/s. The results provide us with the necessary data for analysing the consequences of such events in the context of nuclear power plant safety analyses. In practice, the results can be used to prescribe the boundary conditions for detailed CFD analyses of aircraft impact fires and to validate the simulation tools and methodologies.

The overall shape and speed of the liquid spray was investigated using high-speed video cameras. The images taken from the direction of arrival indicate that the cylindrical projectiles produce a very symmetrical spray. Adding liquid-filled 'wings' to the projectile increased the proportion of liquid leaving in vertical directions. The images taken from the side of the impact indicate that initially the spray is retained at angles of between 0 and 20...40° from the wall tangent. After some distance, the angle of spray propagation gets smaller, presumably due to the one-sided air entrainment. As a result, the global shape of the impact spray is a flat disk spreading in the direction of the target wall tangent. This observation was consistent with the larger scale results in the literature. Behind the leading spray front, the spray was found to consist of sequential waves following each other. It is not clear at the moment if the waves were generated in the eruption process or as a result of the liquid-gas interactions, but they have a clear role in the hydrodynamic process of fast spray penetrating into still air.

The speed of the liquid spray front was determined from the high-speed video images. The initial spray speed ranged between 1.5 and 2.5 times the impact velocity, being 1.7 ± 0.25 on average. The spray front deceleration rate was found to be about 16% when it travelled a distance of one projectile diameter. Dependence of the spray speed on the experimental parameters, such as the impact speed or the projectile wall material, could not be confirmed.

Time series of droplet size and velocity distributions in the spray were successfully measured using two ultra-high-speed cameras. The image sequences at 40 000–100 000 Hz were illuminated with pulsed diode lasers in backlight configuration. A two-camera approach allowed the size and velocity measurement of small and large droplets at the

same time, with a size range of [12–2500] µm. We could, however, visually observe droplets that were even smaller than 10 µm in the images. Droplet concentration was also estimated, although the measurement clearly underestimated the droplet concentration in the dense spray front. It was impossible to analyse all droplets that passed the measurement volume, because the visibility of the measurement volume was often blocked by large liquid fragments.

The measurement results revealed many interesting details in the spray. The ratio of the maximum measured droplet velocity and the impact velocity was near unity for all test cases at the measurement location two metres from the impact point. The droplets within the spray front moved slightly more quickly in the case of the thin-wall projectile in comparison to the thick-wall projectile. Higher impact velocity caused smaller droplets: the mean droplet diameter of 78 µm was obtained with the impact velocity of 97 m/s, whereas at 126 m/s the mean of 39 µm was achieved. The droplet velocities dropped quickly after the spray front and a turbulent flow regime was formed. Plenty of micro-droplets and large droplets were detected, indicating a high collision rate of droplets. All tests included secondary spray fronts that caused the scatter in the measured time trends.

The collected information about the initial droplet direction, speed and size distribution can be used to specify the boundary conditions for the CFD simulations investigating the dynamics of the aircraft impact fires. Such simulations are obviously very challenging, and careful verification and validation processes are needed to ensure the reliability of predictions. The collected information about spray propagation dynamics can be used for validation purposes.

To date, the only liquid to be used is water. More comprehensive validation of the simulation technologies requires well-documented experiments with projectiles filled with a well-characterised hydrocarbon fuel. For the full validation of the spray combustion calculations, experimental sprays should be ignited. The current results form a good basis for designing such experiments, although the safety aspects will certainly pose practical limitations. Other topics of future research include the mechanical conditions leading to the penetration of liquid through the structure, and the characterisation of the sprays in such situations.

Acknowledgements

References

Abbasi, T., Abbasi, S.A. 2007.The boiling liquid expanding vapour explosion (BLEVE): Mechanism, consequence assessment, management. Journal of Hazardous Materials 141, 489–519.

Anghileri, M., Castelletti, L.-M.L., Tirelli, M. 2005. Fluid-structure interaction of water filled tanks during the impact with the ground. Int. J. Impact Engineering 31 (2005), 235–254.

Canny, J. A. 1986. Computational Approach to Edge Detection, IEEE Trans. Pattern Analysis and Machine Intelligence, 8(6), 679–698.

Babinsky, E., and P. E. Sojka. 2002. Modeling drop size distributions. *Progress in Energy and Combustion Science* 28, no. 4, 303–329.

Fasanella EL, Jackson KE. 2001. Crash simulation of a vertical drop test of a B 737 fuselage section with auxiliary fuel tank. Third Triennial International Fire & Cabin Safety Research Conference, Atlantic City, New Jersey, October 22–25, 2001.

Fdida N., Blaisot J-B. 2010. Drop size distribution measured by imaging: determination of the measurement volume by the calibration of the point spread function. Meas. Sci. Technol. 21, 025501.

Field, J.E., Dear, J.P., Ogren, J.E. 1989. The effects of target compliance on liquid drop impact. J. App. Phys 65(2), 533–540.

Jepsen, R., Jensen, K., and O'Hern, T. 2004. Water Dispersion Modeling and Diagnostics for water Slug Impact Test. SEM X International Congress and Exhibition on Experimental and Applied Mechanics. Costa Mesa, Ca, 7–11 June 2004.

Knezevic, K.H. 2002. High-Velocity Impact of a Liquid Droplet on a Rigid Surface: The Effect of Liquid Compressibility. Doctoral Thesis. Swiss Federal Institute of Technology, Zurich. 2002. DISS. ETH NO. 14826.

Kärnä, T., Saarenheimo, A. and Tuomala, M. 2004. "Impact loaded structures". In: SAFIR, the Finnish Research Programme on Nuclear Power Plants Safety. Interim Report, VTT Publications 2272, Espoo 2004, pp. 113–122.

Jepsen, R.A., O'Hern, T., Demosthenous, B, Bystrom, E., Nissen, M., Romero, E., and Yoon, S.S. Diagnostics for liquid dispersion due to a high-speed impact with accident or vulnerability assessment application. Meas. Sci. Technol. 20 (2009), 1–12.

McGrattan, K., McDermott, R., Floyd, J., Hostikka, S., Forney, G., and Baum, H. 2012. International Journal of Computational Fluid Dynamics, 1–13.

Minor, L. G., and Sklansky, J. 1981. The Detection and Segmentation of Blobs in Infrared Images, Systems, Man and Cybernetics, IEEE Transactions 11, 194–201.

Muto, K., Sugano, T., Tsubota, H., Kasai, Y., Koshika, N., Suzuki, M., Ohrui, S., von Riesemann, W.A., Bickel, D.C., and Parrish, R.L. 1989. Full-Scale Aircraft Impact Test for Evaluation of Impact Forces: Part 2: Analysis of Results. International Conference on Structural Mechanics in Reactor Technology 10, Anaheim, CA 1989.

Ouellette NT, Xu H, Bodenschatz E. 2006. A quantitative study of three-dimensional Lagrangian particle tracking algorithms. Experiments in Fluids, Vol 40, pp 301–313.

Reitz, R.D. (1987). Modeling atomization processes in high-pressure vaporizing sprays. Atomisation and Spray Technology 3, pp. 309–337.

von Riesemann, W.A., Parrish, R.L., Bickel, D.C., Heffelfinger, S.R., Muto, K., Sugano, T., Tsubota, H., Koshika, N., Suzuki, M., and Ohrui, S. 1989. Full-Scale Aircraft Impact Tests for Evaluation of Impact Forces: Part 1. Test Plan, Test Method, and Test Results. International Conference on Structural Mechanics in Reactor Technology 10, Anaheim, CA 1989.

Silde, A., Hostikka, S., Kankkunen, A., Hakola, I., and Hyvärinen, J. 2007. Experimental and numerical studies on liquid dispersal from projectile impacting on wall. 19th International Conference on Structural Mechanics in Reactor Technology (SMiRT-19), August 12–17, 2007 Toronto, Canada.

Silde, A., Hostikka, S., and Kankkunen, A. 2011. Experimental and numerical studies of liquid dispersal from a soft projectile impacting a wall. Nuclear Engineering and Design 241, 617–624.

Sugano, T., Tsubota, H., Kasai, Y., Koshika, N., Orui, S., von Riesemann, W.A., Bickel, D.C., Parks, M.B. Full-scale aircraft impact test for evaluation of impact force. Nuclear Engineering and Design 140, 373–385.

Tieszen, S.R. 1997. Post-Crash Fuel Dispersal. Workshop on Aviation Fuels with Improved Fire Safety. Washington DC, 19–20 Nov. 1997. PBD: 1997.

Vepsä, A., Saarenheimo, A., Tarallo, F., Rambach, J.-M., and Orbovic, N. Impact Tests for IRIS_2010 Benchmark Exercise, Journal of Disaster Research, Vol. 7, No.5, 2012, pp. 619–628.